Astron. Astrophys. 349, 801–811 (1999)

ASTRONOMY AND ASTROPHYSICS

A complex bipolar outflow in the Wolf-Rayet BCDG He 2-10

D.I. Méndez[1], **C. Esteban**[1], **M.D. Filipović**[2,3,4], **M. Ehle**[2], **F. Haberl**[2], **W. Pietsch**[2], **and R.F. Haynes**[4]

[1] Instituto de Astrofísica de Canarias, E-38200 La Laguna, Tenerife, Canary Islands, Spain
[2] Max-Planck-Institut für Extraterrestrische Physik, Giessenbachstrasse, D-85740 Garching, Germany
[3] University of Western Sydney, Nepean, P.O. Box 10, Kingswood, NSW 2747 Australia
[4] Australia Telescope National Facility, CSIRO, P.O. Box 76, Epping, NSW 2121 Australia
(dmendez, cel@ll.iac.es; fica, mehle, fwh, wnp@mpe.mpg.de; rhaynes@atnf.csiro.au)

Received 27 January 1999 / Accepted 21 April 1999

Abstract. We present results from multi-wavelength observations of the Wolf-Rayet (WR) blue compact dwarf galaxy He 2-10. These observations include Hα and optical red continuum imaging, high resolution Hα spectroscopy, high resolution radio-continuum mapping at 4.80 and 8.64 GHz and *ROSAT* X-ray observations.

The deep Hα images reveal that the galaxy is surrounded by a complex kiloparsec-scale bipolar superbubble centered on the most intense star forming knot. High-resolution spectroscopy of this feature indicates that it has a complex structure of possibly different kinematic components expanding at velocities from $\leq$50 km s^{-1} up to 250 km s^{-1}. These kinds of outflows are likely to be produced by the mechanical action of stellar winds and supernova (SN) explosions in the intense starbursts that the galaxy hosts. This scenario is consistent with the finding of a steep overall radio spectral index (α=–0.59) that confirms the presence of a large number of supernova remnants ($\sim$3750) in the galaxy. The study of radio spectral index throughout the galaxy shows that the eastern parts have significantly steeper spectra. These radio regions have no counterparts in our Hα or X-ray images.

The X-ray emission extends to a similar scale as the Hα emission. The extensions of the X-ray distribution towards northeast and southwest appears to be well spatially correlated with the position of the bipolar lobes indicating the hot gas is confined inside the bubbles.

The comparison between the energetics of the outflows and the expected mechanical energy released by the supernovae and stellar winds indicates that the large-scale expanding structures can be powered by the massive star population of the galaxy and, therefore, can be considered a galactic wind. Estimates of the escape velocity of the galaxy indicate that part of the large-scale outflows can escape the weak potential well of the galaxy, reinforcing the possibility of a blowout in He 2-10.

Key words: galaxies: individual: He 2-10 – galaxies: kinematics and dynamics – galaxies: starburst – radio continuum: galaxies – X-rays: galaxies – stars: Wolf-Rayet

Send offprint requests to: D.I. Méndez

1. Introduction

Blue compact dwarf galaxies (BCDGs) are essential for understanding fundamental astrophysical problems, such as star formation (SF) and chemical evolution of galaxies. Their observational features (small linear sizes, young stellar population, low metallicity and high gaseous content) indicate that they are poorly evolved objects. Their spectra, dominated by nebular emission lines, are a consequence of the ionization of large amounts of gas by massive stars in starbursts (Sargent & Searle 1970), and are similar to those of H II regions. However, a number of these galaxies show a broad He II 4686 Å spectral feature, related to the presence of WR stars in the ionizing clusters. Because of this, Conti (1991) called them WR galaxies. According to the population synthesis models (e.g. Cerviño & Mas-Hesse 1994; Meynet 1995), the presence of this feature is an indication of the extreme youthness of the burst.

There is direct evidence for a large scale, high velocity flows in the ionized gas associated to some BCDGs. Extensive low-intensity filamentary structures have been detected (using Hα imaging) in more than a dozen of these galaxies, of which, almost half, have been catalogued as WR galaxies (De Vaucouleurs et al. 1974; Meurer et al. 1992; Caldwell & Phillips 1989; Dufour & Hester 1990; Marlowe et al. 1995; Martin 1998). This proportion is large if we compare it with the total ratio of WR to H II galaxies and take into account that surveys have not been devoted specially to WR galaxies. These structures dominate the low-intensity Hα extended emission, given the fact that their morphology is typically filamentary and bipolar, and in most of the cases, aligned with the minor axis of the galaxy. High resolution spectroscopic studies have been reported for some of these galaxies (Meurer et al. 1992; Marlowe et al. 1995, Martin 1998). The structures appear to be hollow cavities with sizes of the order of kpc, expanding with velocities between 25 and 150 km s^{-1}. They could be produced by the combined action of SN explosions and stellar winds leading to the so-called galactic winds (Leitherer 1994).

According to the estimates by Marlowe et al. (1995) and Martin (1998), the energy deposited by the SN explosions together with stellar winds originating from the OB stars in associations can account for the presence of these superbubbles.

Moreover, Stevens & Strickland (1998) carried out a systematic study of the X-ray emission of a sample of WR galaxies. They found that X-ray luminosities for WR galaxies are considerably larger than X-ray luminosities for other galaxies with the same B luminosities concluding that this is a consequence of the higher occurrence of superbubbles in WR galaxies.

Among the BCDGs, He 2-10 is the first emission line galaxy found to exhibit evidence for WR stars in its spectrum (Allen et al. 1976). This is an indication of the presence of an exceptional population of WR stars compared to normal OB stars and so of the extreme youth of the burst.

Henize (1967) first discovered He 2-10 (also known as ESO 495-G021 and PK 248+08) in his Hα survey of the Southern Sky. At that time, he classified He 2-10 as a planetary nebula but Kondratjeva (1972) first indicated its extragalactic nature.

Optical imaging and spectroscopy of He 2-10 has been reported by Johansson (1987), Sugai & Taniguchi (1992) and Corbin et al. (1993; and references therein). They found that the galaxy contains two starburst regions at the center of an elliptical stellar envelope of $\sim$70$''$ diameter. HST UV imaging obtained by Conti & Vacca (1994) reveals that SF activity in this galaxy divides into smaller subunits – probably extremely young globular clusters – probably as the result of an interaction or merger event. This scenario is favoured by Kobulnicky et al. (1995) based on results from detailed CO and H I observations. Also, Davies et al. (1998) supported this scenario based on results from near-infrared observations. They emphasize that the most plausible scenario for He 2-10 is a moderately advanced merger between two dwarf galaxies. On the other hand, Vacca & Conti (1992) found large numbers of WR stars in the two nuclear starburst regions, mostly in the brightest one (named A after Corbin et al. 1993). Méndez & Esteban (1997) carried out high resolution echelle observations of the object detecting the presence of asymmetric broad low-intensity wings in the profiles of the brightest emission lines which extended farther out from the star forming knots, showing linear dimensions of even $\sim$1 kpc. The maximum velocity of the gas was about 340 km s^{-1}. These authors conclude that superbubble blowout expanding over a cloudy medium can explain these observational properties.

He 2-10 was the first BCDG detected at radio-continuum frequencies (Allen et al. 1976). Detection was made with the Parkes radio telescope at several frequencies. From those early radio observations, Allen et al. (1976) found that He 2-10 shows non-thermal radio spectra with spectral index $\sim -0.60 \pm 0.15$. Due to a large observing beam size their detection of He 2-10 was quoted as – unresolved point source with diameter of $< 2'$. They found relatively high flux densities (e.g. S_{6cm}=45$\pm$10 mJy) in all radio frequencies. Recent radio-continuum studies of the northern hemisphere BCDGs (Klein et al. 1991) showed that these objects have about 10 times higher radio-to-optical luminosity ratio than normal spiral galaxies and they have a steeper radio spectrum indicating low radio frequency breaks. Also, Klein et al. (1991) successfully separated non-thermal from thermal emission in most observed BCDGs. In an attempt to understand the high radio-continuum luminosity of He 2-10, Allen et al. (1976) estimated that about 5000 supernova remnants (SNRs) contribute to the non-thermal emission of this BCDG. Their finding is rather high and here we will revise this estimate with regard to the galaxy improved flux and distance estimate (Sect. 3.3).

The *ROSAT* PSPC/HRI X-ray emission from He 2-10 was reported by Hensler et al. (1997), Dickow et al. (1996), Stevens & Strickland (1998) and Papaderos & Fricke (1998). Hensler et al. (1997) indicate that abundances taken from type II SN nucleosynthesis provide a better fit to the *ROSAT* PSPC X-ray spectrum of the galaxy in comparison with a Raymond-Smith spectrum with purely solar abundances.

Assuming a uniform Hubble flow with H_o=75 km s^{-1} Mpc^{-1} and given the value of 895 km s^{-1} for the recession velocity of the object (Méndez & Esteban 1997), He 2-10 lies at 11.9 Mpc. At this distance, the spatial scale is 57.7 pc arcsec^{-1}.

2. Observations and data reduction

2.1. Optical imaging

Optical observations were carried out on 4 February 1997 at the 2.56-m Nordic Optical Telescope (NOT) of the Roque de los Muchachos Observatory at La Palma (Canary Islands, Spain). We obtained Hα and adjacent continuum high-resolution CCD images using the StanCam Camera with a TEK CCD detector (1024 $\times$ 1024 pixels) with a pixel size of 24 μm^2 and a spatial resolution of 0.176$''$ pixel^{-1}. The narrow band filters for the Hα and red-continuum images (centered at 6563 and 6640 Å respectively and with a FWHM of 50 Å in both cases) were selected taking into account the red-shift of He 2-10 estimated from Méndez & Esteban (1997). Three exposures of each filter (of 600 s for the Hα image and 500 s for the continuum one) were added to obtain a good signal-to-noise and an appropriate removal of cosmic rays in the final images. The images were bias subtracted, flat-fielded and flux calibrated following standard procedures. The absolute flux calibration was achieved using short exposures of the calibration star BD+75^{o}325 (Oke 1990). The images were also sky subtracted and corrected for atmospheric and interstellar extinction using spectroscopic data taken from Vacca & Conti (1992). All the reduction process was done with the IRAF[1] package. The Hα image was corrected for [NII] emission taking into account the [NII]/Hα ratio also from Vacca & Conti (1992). The mean seeing during the observations was about 1$''$. The log of all the observations can be found in Table 1.

2.2. IACUB high resolution Hα spectra

Observations were carried out on 23 February 1998 with the IACUB spectrograph at the Cassegrain focus of the 2.56-m NOT telescope. Technical specifications about the IACUB high-resolution spectrograph can be found in McKeith et al. (1993).

[1] IRAF is distributed by NOAO which is operated by AURA, Inc., under cooperative agreement with NSF

A slit covering $45'' \times 0.9''$ was used. We used a narrow-band filter (FWHM of 50 Å) centered at 6563 Å in order to isolate the order corresponding to the Hα emission line of the galaxy. The spectrograph gives a reciprocal linear dispersion of 1.74 Å mm^{-1} at Hα. We used a Thompson 1024 $\times$ 1024 pixels CCD with a pixel size of 19 μm^2 with a binning $\times$ 2. At the wavelength of Hα, each binned pixel corresponds to $0.278''$ in the spatial direction and to 0.066 Å in the spectral direction (i.e. the effective resolution in velocity is 9 km s^{-1}).

Exposures of a Th-Ar lamp were taken for wavelength calibration. No flux calibration was intended.

2.3. Radio-continuum mapping

Radio-continuum observations of He 2-10 were made on 15 May 1998 with the Australia Telescope Compact Array (ATCA). The array was in the 6C antenna configuration, with baselines ranging between 153 and 6000 m. All observations were made simultaneously at 4.80 and 8.64 GHz (λ=6.3 and 3.5 cm). Using this baseline configuration at ν=4.80 and 8.64 GHz we achieved a resolution of $2''$ and $1''$ respectively. This was considered as the best angular resolution with which to study this BCDG in detail, ensuring at the same time sufficient sensitivity to any extended emission component. Primary flux calibration was achieved using PKS 1934-638 and for the phase calibration we used the secondary calibrator PKS 0826-373. Data reduction was performed using the MIRIAD software package (Sault & Killeen 1998).

2.4. ROSAT HRI and PSPC observations

The *ROSAT* archive contains a total of three observations centered in the field of He 2-10. Details on the *ROSAT* mission can be found in Trümper (1983) and Pfeffermann et al. (1986). Two observations were carried out with the HRI detector (energy range 0.1–2.4 keV) in November 1994 and November 1995 and one PSPC observation was performed in May 1992. For more details on all observations used for the study presented here see Table 1.

3. Results

3.1. Narrow-band imaging

In Fig. 1 we show a contour plot (white) superimposed to a gray scale representation of the continuum-subtracted Hα image of He 2-10. At high intensities, the net Hα emission is distributed in two different star-forming knots (#1 and #2). Also, we notice the presence of two more star-forming knots located about 1 kpc to the southwest of the centre of the galaxy (#3 and #4). All these selected regions are labelled in Fig. 1. Apart from the individual star-forming knots mentioned above, it is possible to find more enhancements in the Hα emission that could also be identified as star-forming knots. However, we have not included them in our detection because they are likely condensations in the borders of bubble-like structures and not real star-forming knots, since there is almost no emission in the continuum (see Fig. 2) in these regions. This hypothesis is in good agreement with the morphology of the W(Hα) map that we present in Fig. 3. Also, knots #3 and #4 do not have a continuum counterpart either, but

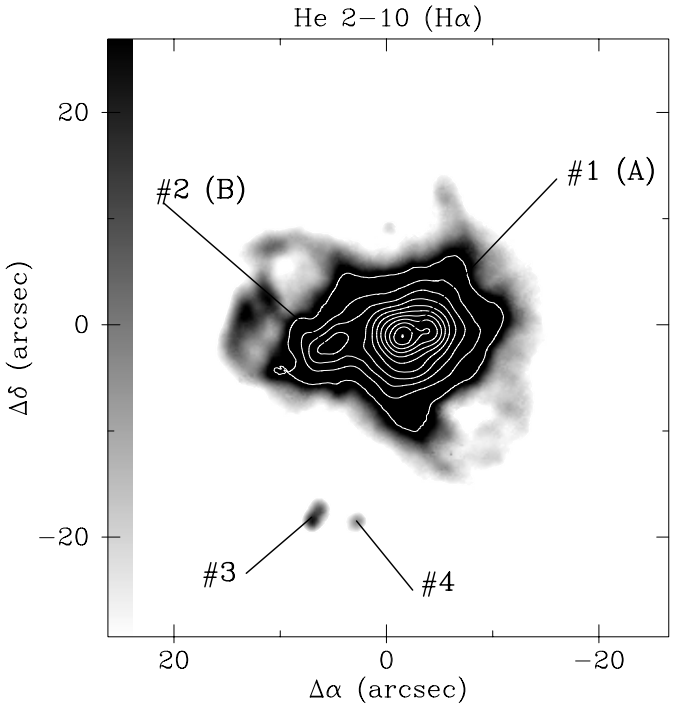

Fig. 1. Contour plot (white) superimposed to a linear gray-scale image of the continuum-subtracted Hα image of He 2-10. Labels refer to the different star-forming knots analysed here. North is at the top and East on the left.

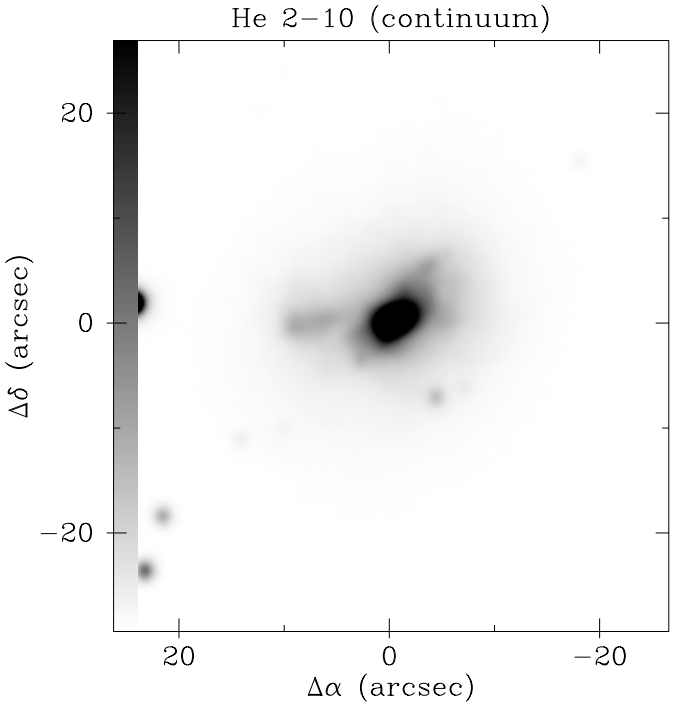

Fig. 2. Linear gray-scale representation of the red continuum image of He 2-10. North is at the top and East on the left.

Table 1. Summary of the multi-frequency observations of He 2-10 used in this study.

Optical Observations	Date	P.A. (°)	Exposure Time (s)	Spatial Sampling ($''$ pix^{-1})	Spectral Resolution (Å pix^{-1})	λ_C Filter (Å)
IACUB	98/02/23	49	3×1800	0.28	0.066	6563
Spectroscopy	98/02/23	90	3×1200	0.28	0.066	6563
Narrow-band	97/02/04	...	3×600	0.176	...	6563
Imaging	97/02/04	...	3×500	0.176	...	6640

X-ray Observations	Date	Sequence Number	R.A. (J2000)	Dec (J2000)	Exposure Time (s)
ROSAT PSPC	14/05/92	600211p	$08^h36^m14^s$	–26° 24′ 36″	9220
ROSAT HRI	12/11/94	600700h	$08^h36^m14^s$	–26° 24′ 36″	20326
ROSAT HRI	24/11/95	600700h-1	$08^h36^m14^s$	–26° 24′ 36″	18972

Radio-Continuum Observations	Date	Frequency (GHz)	Beam Size ($''$)	rms Noise (mJy beam^{-1})	Flux Calibrator	Phase Calibrator
ATCA	98/05/15	4.80	2	0.15	PKS B1934−398	PKS B0826−373
ATCA	98/05/15	8.64	1	0.15	PKS B1934−398	PKS B0826−373

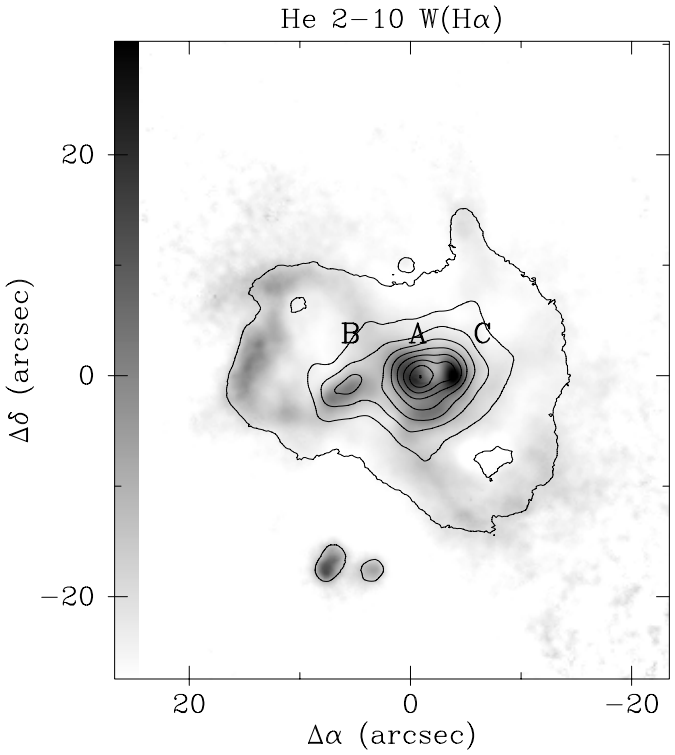

Fig. 3. Hα equivalent width map of the central regions of He 2-10. The continuum-subtracted Hα image is superposed as isocontour plot. Color scale is linear (white: minimum, 38 Å; black: maximum, 410 Å). North is at the top and East on the left.

due to their round-like morphology and the fact that they are not related with the bubble-like structures we consider that they are real star-forming knots.

The apertures used for flux extraction of the different knots detected in the continuum-subtracted Hα image were defined using the FOCAS IRAF package. For a detailed description of this task, see Méndez et al. (1999). Data concerning Hα luminosity, the number of ionizing photons, the mass of ionized hydrogen and the equivalent width of Hα, W(Hα), of the different knots can be found in Table 2. We can also find in Table 2 values related to the whole galaxy, calculated with an aperture larger than its actual size. It must be mentioned here that when calculating these integrated quantities of the whole galaxy, only those pixels whose number of counts was higher than 3σ of the background ($\sim 8.2 \times 10^{34}$ erg s^{-1}) were taken into account. The lower value of the total W(Hα) compared with the values of the knots #1 and #2 results from the fact that the continuum emission is not exactly spatially coincident with the Hα one. For the calculation of the number of ionizing photons and the mass of ionized hydrogen we used the values of the electron density and temperature given by Vacca & Conti (1992). Poissonian uncertainties in the Hα fluxes are always less than 1.5% of the value of the flux. In the case of the W(Hα) values, Poissonian uncertainties are always less than 3%.

As it had been reported before, the brightest knots (#1 and #2, A and B respectively in the nomenclature adopted by Corbin et al. 1993) are located in the nuclear region. Knot A and B account for 66% and 2% respectively of the total Hα emission of the galaxy. Knot A has an Hα luminosity a factor 13 higher than 30 Doradus, a giant HII region in the LMC and a diameter about 1.5 times larger.

Knots #3 and #4 correspond to the blob of Hα emission already reported in Beck & Kovo (1999), that now can be resolved in two different star-forming knots. These two knots are located at the end of the CO tail reported by Kobulnicky et al. (1995). This supports the interpretation of Beck & Kovo (1999) that these knots are in a cluster of young stars formed at the end of the tail. Furthermore, we notice that the main axis of the double knot points to the centre of the galaxy in the direction of the CO tail.

Using Kennicutt (1988) and the value of the total integrated Hα luminosity we can derive a number of 1.1×10^6 M$_\odot$ for the mass of the ionizing stars (10–100 M$_\odot$) in the whole

Table 2. Results of Hα aperture photometry. Luminosities and derived magnitudes are calculated assuming a distance of 11.9 Mpc.

Region	RA (J2000)	Dec (J2000)	log[L(Hα)] (cgs)	log[Q(H^o)]	log($M_{H\,II}/M_\odot$)	$-$W(Hα) (Å)
#1(A)	$08^h36^m15.22^s$	$-26^\circ\,24'\,34.3''$	41.31	53.31	6.13	225
#2(B)	$08^h36^m15.72^s$	$-26^\circ\,24'\,35.0''$	39.80	51.80	4.62	175
#3	$08^h36^m15.92^s$	$-26^\circ\,24'\,51.3''$	38.78	50.78	3.60	160
#4	$08^h36^m15.62^s$	$-26^\circ\,24'\,51.9''$	38.47	50.47	3.29	110
Total	–	–	41.49	53.49	6.31	120

galaxy. This value of the mass corresponds to the presence of about 6200 O5V stars in the whole galaxy (assuming a value of $Q(H^o)$=5×10^{49} photons s^{-1} per star). It is also consistent with the number of equivalent O7V stars obtained by Vacca & Conti (1992) for the whole integrated spectrum of the two nuclear knots ($\sim$ 4600 stars) from the comparison of Hβ luminosity and the number of WR stars calculated from the integrated flux of the He II λ4686 Å emission line.

At low intensities (Fig 1), as it has already been reported by Papaderos & Fricke (1998), the presence of two bubble-like structures in the northeast direction around knot A is apparent which resemble the limb brightened edges of a polar outflow. These structures extend out to $\sim$16$''$ from knot A ($\sim$925 pc) which is in the range of the sizes of superbubble structures found in brighter and closer galaxies (Marlowe et al. 1995, Martin 1998). Moreover, another shell structure is detected to the southwest of knot A with a similar shape and size to that of the northeast structure.

On the other hand, the region of maximum W(Hα) does not coincide with the region of maximum Hα emission (see Fig. 3) but it is displaced a few arcsecs to the west. This behaviour suggests that the younger parts of the galaxy are not exactly at the center of knot A, a fact that is in total agreement with the results from MIR observations for this galaxy reported by Sauvage et al. (1997), who state that their region C [located at the west of knot A, well detected in the MIR and coincident with our region of high W(Hα)] is younger than knot A. In our case, we find that the W(Hα) of this region is slightly higher than the value measured at the center of region A. In fact, we have obtained the W(Hα) of the most central regions of A and C (taken a circular aperture of the size of the seeing disk) finding that W(Hα) is $-$360 Å for region C and $-$320 Å for region A, in both cases higher than in region B (its W(Hα) is $-$175 Å, see Table 2).

Following Leitherer & Heckman (1995) and taking into account the value of the W(Hα) of the different knots, it is possible to estimate their age. Assuming a Salpeter inital mass funtion (IMF)[2] with an upper cut-off of 100 $M_\odot$ and a metallicity of 0.1 $Z_\odot$ for knot A and of 0.25 $Z_\odot$ for knot B [3], we estimate an age of about 5 Myr for knot A and B.

[2] The results are very similar for a Scalo IMF.

[3] These metallicities are assumed in order to compare with the grid of models available. Actually, the metallicities obtained by Vacca & Conti (1992) are 0.14 $Z_\odot$ and 0.48 $Z_\odot$ for knot A and B respectively. In any case, the uncertainty caused by this assumption is not very high since there is no significant variation in the models for different metallicities in this range.

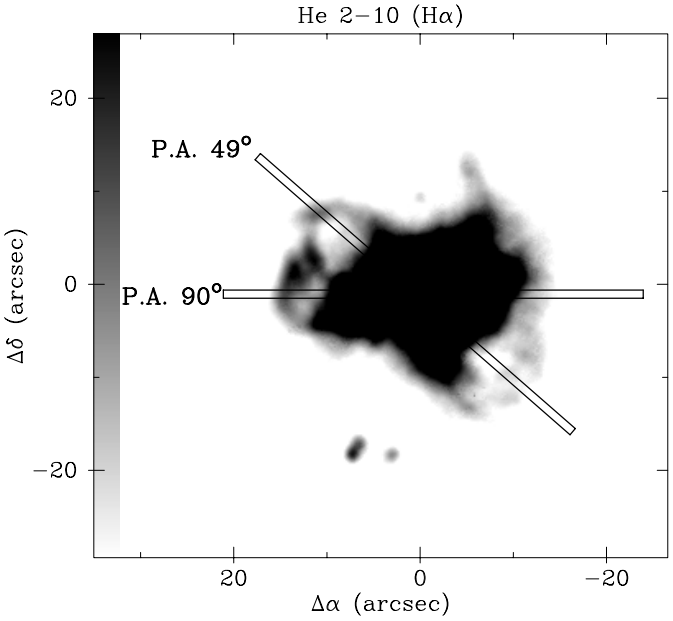

Fig. 4. Slit positions for high resolution spectroscopy. The gray-scale represent the continuum-subtracted Hα image. North is at the top and East on the left.

The current star formation rate (SFR) of the whole galaxy (related to the past $\sim 10^7$ yr, see Gallagher et al. 1984) calculated from the Hα integrated luminosity (assuming a Salpeter IMF with an upper cut-off of 100 $M_\odot$ and a lower one of 0.1 $M_\odot$, Gallagher et al. 1984) turns out to be 4.48 $M_\odot$ yr^{-1}.

3.2. High resolution spectra

Fig. 4 shows the two slit positions observed for He 2-10. These two different P.A.s were chosen in order to study the kinematics of the bubble-like structures detected in the continuum-subtracted Hα image.

In Fig. 5 we present the two-dimensional Hα spectrum for a P.A. of 90°. The vertical bars show the different regions of the spectrum that have been extracted for analysis.

Analysis of the emission line profiles was performed via Gaussian fitting making use of the Starlink DIPSO software (Howarth & Murray 1990). For each single or multiple Gaussian fit, DIPSO gives the fit parameters (radial velocity centroid,

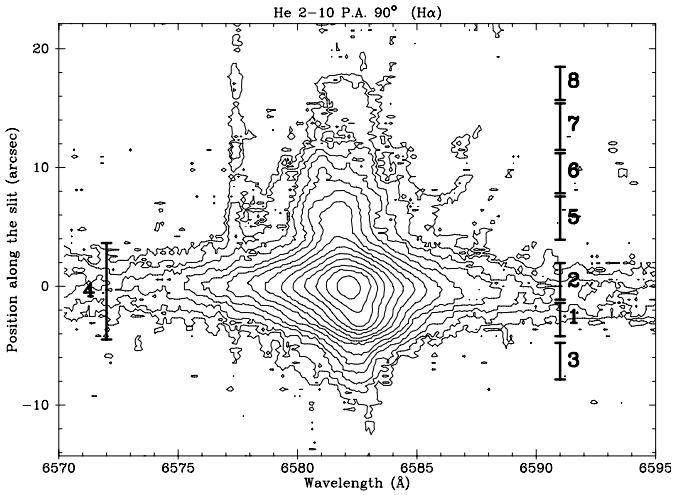

Fig. 5. Contour plot of the two-dimensional Hα profile of He 2-10 for P.A. 90°. The different subregions selected along the slit are indicated and labeled. The top of the plot corresponds to the E.

Gaussian sigma, FWHM, etc.) and their associated statistical errors.

We find, as in the case of previous high-resolution spectral observations of the object (Méndez & Esteban 1997), the presence of broad low-intensity wings in all the regions where a Gaussian fit was possible. There is a sky line at ∼6577.5 Å superposed on the blueshifted wing. Due to the optical design of the spectrograph, the transmission is not homogenous along the spatial direction of the slit, a fact that could not be corrected with internal flat-fields. This problem prevented a proper subtraction of the sky line.

There is a slight difference (∼20 km s^{-1}) in the velocity of the centroid for the central region (region 2, v_{hel}∼852 km s^{-1}) which corresponds to knot A and the enhanced emission region to the east (region 5, v_{hel}∼833 km s^{-1}) which corresponds to knot B. The external regions to the west (regions 1 and 3) present a v_{hel}∼868 km s^{-1}. The mean value of the velocity of the centroid for the brightest regions (region 4) is 857 km s^{-1}, a value slightly lower than 895 km s^{-1}, as found by Méndez & Esteban (1997).

In Fig. 5, we detect the presence of residual low-intensity wings in the brightest regions (knot A, our region 2). The maximum velocities of these residuals are −335 km s^{-1} in the red and +355 km s^{-1} in the blue, and extend about 500 pc, values consistent with the results by Méndez & Esteban (1997).

The full width at half maximum (FWHM) of the Hα profile is very constant along the slit length, varying between 100 and 130 km s^{-1} (corrected for the instrumental profile), velocities which are clearly super-thermal. This large FWHM, the absence of clear line-splitting, and the general non-Gaussian shape of the Hα emission profile indicate the complex kinematics of the ionized gas along a given line of sight. The spatial extension of the broad Hα emission to the east coincides with the bubble-like structure in the continuum-subtracted Hα image in this direction. This spatial coincidence indicates that the observed kinematics could be certainly associated with the superbubble. The average value of FWHM of about 130 km s^{-1} in regions 5 and 6 (those more clearly related with the superbubble) indicates maximum expansion velocities for the bulk of the gas of the order of 50–60 km s^{-1}. If we have a simple "academic" bubble expanding at such velocity, we could be able to see a clear line-splitting at our spectral resolution. Therefore, the observed line profiles suggest an intricate structure of multiple shells or supershells expanding with different velocities. In this sense, the Hα image also shows a complex morphology of, at least, two intersecting bubbles at the eastern edge of the ionized gas distribution. Martin (1998) in her extensive study of outflows in dwarf galaxies, has shown that multi-shell structures (in some cases overlapping) of ionized gas are very common in this kind of galaxies.

Up to the east, in Fig. 5, the signal-to-noise is very low but, apart from the central broad component (with a v_{hel}∼840 km s^{-1}) it is possible to detect a peak of emission redshifted ∼245 km s^{-1} with respect to the central regions and located ∼10–14″ to the east of knot A (regions 6–7). It is possible to interpret this emission feature as partial segments of the receding side of an expanding superbubble. If this is the case, the apparent absence of a blueshifted component (that should be brighter) could be explained as a geometrical effect as in the case of some bipolar planetary nebulae observed at a given P.A. (see for instance P.A. 51° in NGC 6357, Cuesta et al. 1995). In fact, due to the angle of inclination of the polar flow, the approaching side of the bubble could be overlapped with the brighter central component around the systemic velocity of the galaxy (and perhaps contributing to the complex profile of this component). Similar kinematic features have been observed in the dwarf galaxies NGC 3077 (region A) and NGC 1569 (region A) by Martin (1998).

In Fig. 6 we present the two-dimensional Hα spectrum for P.A. 49°. The vertical bars show again the different regions of the spectrum that have been extracted for analysis. We find again that the broad low-intensity wings extend over the brightest regions as in the case of P.A. 90° reaching a linear size of 600 pc. The maximum velocities vary between −315 km s^{-1} and +310 km s^{-1}. The mean heliocentric velocity for the centroid (regions 1 and 2) in the central regions is ∼855 km s^{-1}. This value becomes slightly lower when we move to the northeast (∼ 835 km s^{-1} for region 3).

Up to the east, we detect, as in P.A. 90°, a secondary emission peak redshifted ∼250 km s^{-1} (regions 4 and 5) with respect to the central regions and located again ∼10–14″ to the east of knot A, inside the position of the bubble-like structure detected in the Hα image. This feature could be related to the similar kinematical structure found in the other slit position, and could correspond to a segment of an extended polar superbubble.

As in the case of P.A. 90°, the extended emission to the northeast of the center of the galaxy (regions 3 to 6) shows a broad and complex profile. The FWHM of the Hα line varies from 70 to 140 km s^{-1} indicating that the kinematics of the ionized gas is also complex in this P.A. However, in this case we find a decrease of the FWHM in the external regions (regions 4 to 6) with values of 145 km s^{-1} (region 4), 123 km s^{-1} (region 5), and 67 km s^{-1}

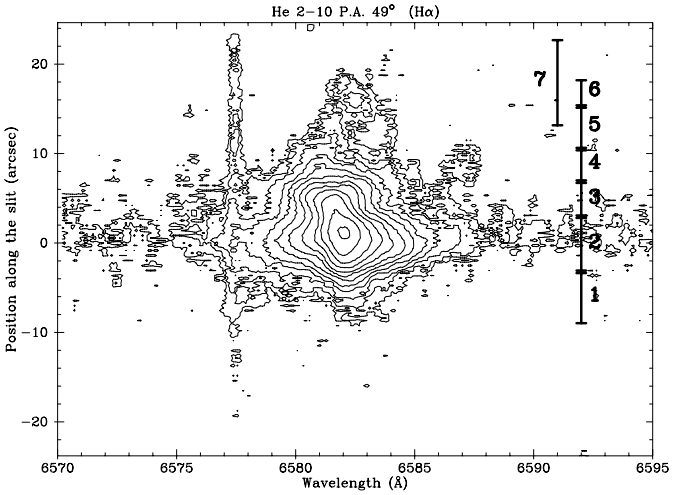

Fig. 6. Contour plot of the two-dimensional Hα profile of He 2–10 for P.A. 49°. The different subregions selected along the slit are indicated and labeled. The top of the plot corresponds to the N-E.

(region 8). This behaviour suggests the presence of a Doppler ellipse. We detect a line-splitting in the regions 6 and 7. We find a brighter central component with a $v_{hel}\sim$865 km s^{-1} (near the systemic velocity of the galaxy) together with a lower intensity component with a $v_{hel}\sim$940 km s^{-1}. Because of the low signal-to-noise of the spectrum, we can not conclude whether the component at 940 km s^{-1} corresponds to: i) the receding side of a bubble which approaching face is the brightest component at 865 km s^{-1} or, ii) the approaching side of the superbubble related with the high velocity feature at $\sim$250 km s^{-1}. The first possibility seems favoured due to the possible presence of a Doppler ellipse commented above.

Despite the clear presence of the bubble-like structure to the southwest of the central knot A in the Hα image, we do not detect any remarkable feature in the corresponding part of the two spectra (nor in the blue, neither in the red). This fact could be due to:

i) The faintness of the emission in this region (in fact the emission is weaker than in the northeast);
ii) The lower transmission of the spectrograph optics in this region of the slit (in fact, it can be seen that the sky line at $\sim$6577.5 Å is also fainter in this region).

Therefore, more observations are needed to determine the kinematics of the shells and bubbles which are clearly seen in this region of the Hα image.

3.3. He 2-10 at radio-continuum frequencies

Radio-continuum observations of BCDG's are generally used for tracing non-thermal emission from these objects. The radio-continuum image of Kobulnicky et al. (1995) at 21 cm (synthesized beam of $11.3''\times 9.6''$) shows only one unresolved knot in the central (optical) area of the galaxy.

Here, in Figs. 7a and 7b, we present our radio-continuum images of He 2-10 overlaid on top of the gray scale Hα image. Both radio images were smoothed to the same resolution ($2''\times 2''$) for a calculation of the spectral index. The r.m.s. noise in both images is σ=0.15 mJy. At both frequencies we can see resolved structures in the central part of the galaxy. Knots A and C seen in optical images correspond to two bright central regions in our radio-continuum images (sources He 2-10 RC1 and He 2-10 RC2).

We distinguish four major peaks in our radio images and estimate their positions, integrated flux and spectral index (for more details see Table 3). Fluxes are not extracted directly but after fitting an elliptical gaussian model to every source of the radio continuum images[4] and then, calculating all the flux contained inside every gaussian. This was also the procedure to calculate the total flux of the galaxy. This way of extracting fluxes after gaussian fittings causes that the sum of the fluxes of the four major sources detected is slightly larger than the flux corresponding to all the galaxy (see Table 3). The spectral index α is defined by the relation $S_\nu \sim \nu^\alpha$, where S_ν is the integrated flux and ν the frequency. We find an overall spectral index of α=-0.59 ± 0.05 for He 2-10 which is in agreement with estimates by Allen et al. (1976). We note that the radio-continuum regions towards the east (He 2-10 RC3 and He 2-10 RC4) have significantly steeper spectra indicating that more non-thermal emission is concentrated there. Therefore, these two eastern radio-continuum knots must contain large contributions of the non-thermal emission from SNRs. Furthermore, the central most luminous region (He 2-10 RC1) compares with the LMC's most luminous H II region – 30 Doradus. As well as 30 Doradus, He 2-10 RC1 (Knot A) has a somewhat flater spectrum than "ordinary" SNRs indicating that non-thermal emission probably originates from SNRs embedded into thermal H II regions. Also, our radio images show that the radio-continuum extension towards the East is not aligned with either optical, H I or CO emission.

Following the formulae given in Pottasch (1984) and considering a value of the electron temperature of 11200 K (Vacca & Conti 1992) together with the value of the Hα flux of the whole galaxy, we can derive the contribution from thermal emission to the radio fluxes at 4.8 and 8.64 GHz. These values turn out to be 2.4 and 2.3 mJy for 4.8 and 8.64 GHz respectively. These thermal fluxes correspond to the 7.9% and 10.7% of the total values of the radio fluxes at 4.8 and 8.64 GHz respectively. As we can see, most of the emission, as it was already suspected, is non-thermal. Just to check coherence, we calculated the spectral index corresponding to the whole galaxy after correcting from these thermal emissions, obtaining a value of -0.64, which is within the uncertainty of the value presented in Table 3.

Comparing the total radio-continuum luminosity of He 2-10 (see Table 3) with that of the LMC (Haynes et al. 1991) we estimate a number of $\sim$3750 SNRs in the galaxy, a value lower but of the same order as the 5000 SNRs found by Allen et al. (1976). Considering an age of 5 Myr for the burst, we estimate a SN rate of 7.5×10^{-4} SN yr^{-1}. Following the calculations by Esteban & Peimbert (1995), these numbers are consistent with

[4] This was the criterion adopted in order to discern which is the actual extension of each source.

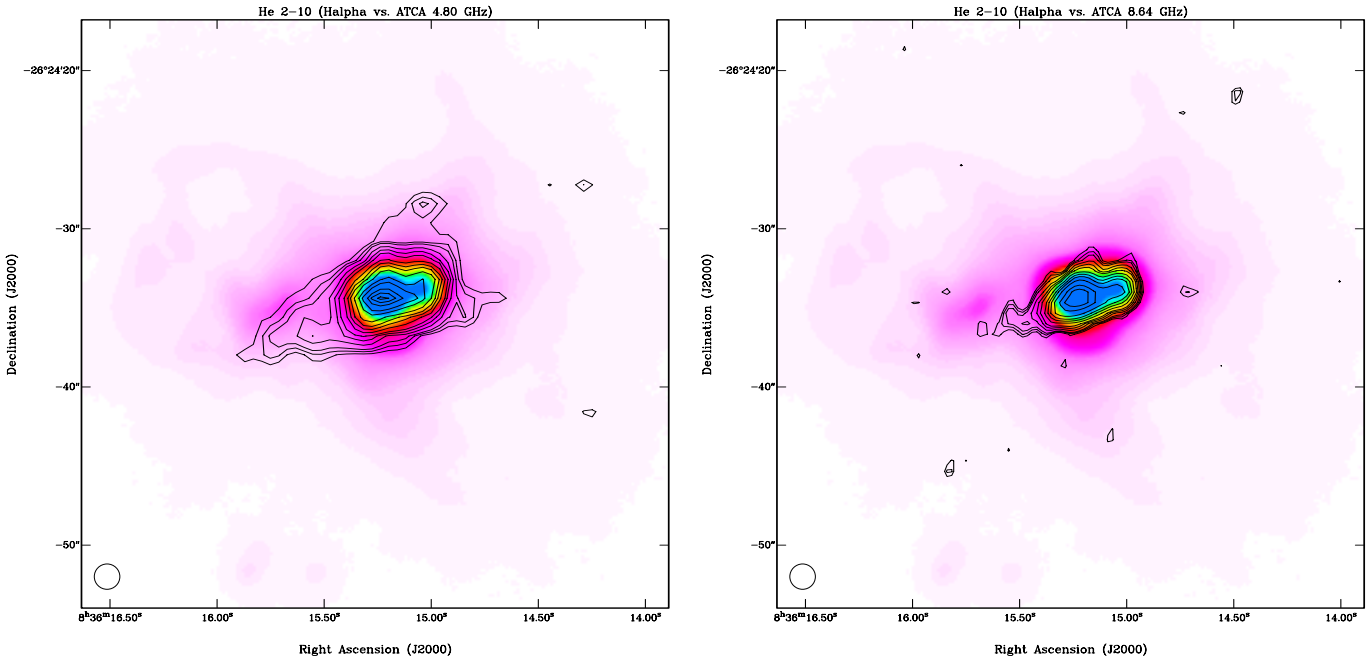

Fig. 7a and b. Radio-continuum images of He 2-10 (contours) at 4.80 GHz (left – **a**) and 8.64 GHz (right – **b**). Gray scale image in background is Hα. The synthesized beam at both images is $2'' \times 2''$(lower left corner) with r.m.s. noise (1σ) of 0.15mJy. Contours are 2σ, 2.5σ, 3σ, 4σ, 5σ, 6σ, 8σ, 10σ, 12σ, 15σ, 20σ, 25σ, 30σ, 35σ and 40σ.

Table 3. The list of radio-continuum sources found in the field of He 2-10. An elliptical gaussian model was fitted to every source in order to estimate the integrated fluxes.

Source Name	R.A. (J2000)	Dec (J2000)	$S_{4.80\ \mathrm{GHz}}$ (mJy)	$S_{8.64\ \mathrm{GHz}}$ (mJy)	$\alpha \pm \Delta\alpha$
He 2-10 RC1	$08^h36^m15.22^s$	$-26^\circ\ 24'\ 34.3''$	15.6	13.9	–0.20±0.12
He 2-10 RC2	$08^h36^m15.06^s$	$-26^\circ\ 24'\ 33.9''$	9.3	7.0	–0.48±0.19
He 2-10 RC3	$08^h36^m15.53^s$	$-26^\circ\ 24'\ 35.8''$	3.5	1.9	–1.13±0.29
He 2-10 RC4	$08^h36^m15.68^s$	$-26^\circ\ 24'\ 36.7''$	3.0	1.4	–1.30±0.32
He 2-10 (tot)	$08^h36^m15.19^s$	$-26^\circ\ 24'\ 34.3''$	30.3	21.4	–0.59±0.05

the expectations for the number of O stars derived (6200 O5V), the age of the burst (5 Myr) and a "normal" value of the slope of the initial mass function.

Using the estimated spectral index of the galaxy, we derive a radio-continuum flux of 62.7 mJy at 1.4 GHz. Applying the formula given in Cram et al. (1998) we obtain a SFR ($M \geq 5\ M_\odot$) of 0.27 $M_\odot\ yr^{-1}$, a value considerably lower than the one obtained from the Hα emission. This discrepancy dissapears if we compare with the current SFR from the Hα emission calculated using an "extended" Miller-Scalo IMF with an upper cut-off of 100 $M_\odot$ and a lower one of 5 $M_\odot$ (the same IMF and mass interval used in the calculations by Cram et al. 1998) instead of a Salpeter IMF with an upper cut-off of 100 $M_\odot$ and a lower one of 0.1 $M_\odot$ (as it has been done in Sect. 3.1, following Gallagher et al. 1984). We obtain this way a value of 0.54 $M_\odot\ yr^{-1}$ for the current SFR. Furthermore, according to Pérez-Olea & Colina (1995), the previous value of the SFR calculated from radio-continuum observations can change within a factor of $\sim$2 if we consider that the non-thermal emission from galaxies may be dominated by radio SNe with lifetimes of 100 yr or so, rather than remnants with lifetimes exceeding 20000 yr.

3.4. X-ray emision of He 2-10

Preliminary results from an X-ray investigation of He 2-10 have been presented by Hensler et al. (1997), Dickow et al. (1996) and Stevens & Strickland (1998). They used the *ROSAT* PSPC data to investigate X-ray spectra of He 2-10 while Papaderos & Fricke (1998) compared the *ROSAT* HRI soft X-ray image with various optical images. However due to the systematic boresight error of $\sim 7''$ in the ROSAT data, positional alignment could only be done to this accuracy.

In this work we use an X-ray source located about $4.4'$ North-West of He 2-10 and which we name as RX J0836.0-2621 as reference for positional calibration. A summary of X-ray sources and their properties from the *ROSAT* HRI image is given in Table 4. The position of RX J0836.0-2621 corresponds to a bright star (m_v=10.56) in the Tycho catalogue (Hog et al. 1997).

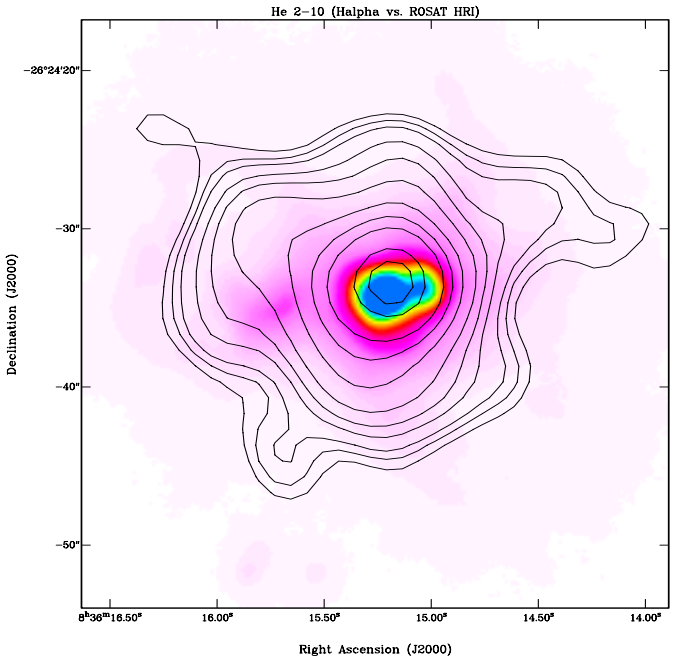

Fig. 8. The ROSAT HRI image (contours) of He 2-10 overlaid on top of the gray-scale Hα image. The average background is 1.7×10^{-4} cts s^{-1} arcmin^2. Contours are 6, 7, 8, 10, 12, 15, 20, 25, 30, 40 and 45 $\times10^{-4}$ cts s^{-1} arcmin^2.

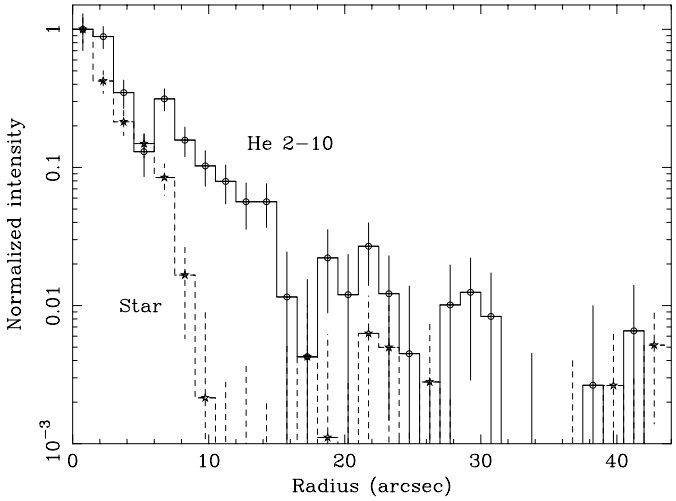

Fig. 9. The radial profile (histogram) of He 2-10 represented with circle (solid line) and RX J0836.0-2621 represented with star (dashed line).

Table 4. *ROSAT* HRI sources found in the field of He 2-10

Source Name	RA (J2000)	Dec (J2000)	Rate (10^{-4}cts/s)
He 2-10 RC1	$8^h36^m15.21^s$	–26° 24′ 33.7″	44±4
RX J0836.0-2621	$8^h36^m00.36^s$	–26° 21′ 38.2″	33±3

We used the accurate (<0.03″) optical position to correct the alignment of our *ROSAT* HRI image. The applied shift is 5.5″. The remaining positional uncertainty is dominated by the residual statistical error in the *ROSAT* HRI image of ∼1.5″. In Fig. 8 we present the *ROSAT* HRI image of He 2-10. For the image we combined the data of both HRI observations (Table 1).

To investigate a possible angular extent of He 2-10 in the *ROSAT* HRI image we compared the ring-integrated radial profile of this BCDG with that of the star RX J0836.0-2621, which should represent the point spread function of the instrument. The radial profiles are given in Fig. 9 and clearly show extended X-ray emission from He 2-10. The extent at 5% of the maximum intensity is ∼7.3″ (radius). Within ∼5″ the radial profile of He 2-10 is consistent with that of RX J0836.0-2621, suggesting the existence of an unresolved source (or close sources) in the center of the X-ray emission.

The location of the main He 2-10 X-ray peak is within 0.7″ of knot A seen in the radio-continuum and Hα maps (i.e. within the remaining HRI positional error, after correction, the central X-ray peak coincides with knot A). The X-ray emission extends on a similar scale than the Hα emission. Two extensions of the X-ray emission towards northeast and southwest appear to be well spatially correlated with the position of the bipolar lobes indicating that the hot gas is confined inside the bubbles. On the other hand, we can see a few low-emission spurs (one towards the northwest and another one towards the southeast in the direction to knots #3 and #4 and the CO tail). Localized plumes or spurs of X-ray emission extending beyond the Hα emission have been observed in other starburst galaxies as NGC 3079 (Pietsch et al. 1998), Mrk 266 (Wang et al. 1997) and NGC 4666 (Dahlem et al. 1997) and could be related to the outflow or leakage of hot gas in those particular zones.

To calculate the total X-ray luminosity (0.1–2.4 keV) from He 2-10 we use the X-ray spectrum derived from the *ROSAT* PSPC data and fit a simple bremsstrahlung model with photoelectric absorption by matter of cosmic abundance. The best fit temperature is 0.45 keV with absorption of 1.8 10^{21} cm^{-2}. The error on the absorbing column density is large (8.4 10^{20} cm^{-2} – 4.7 10^{21} cm^{-2}) which leads to a large uncertainty on the derived intrinsic X-ray luminosity of L_x=8.5×10^{39} erg s^{-1} to 8.5×10^{40} erg s^{-1}. From the derived temperature and luminosity it is not clear whether the X-rays originate from hot gas and/or a number of X-ray binaries. From an ASCA observation of He 2-10, Ohyama & Taniguchi (1998) also conclude that high mass X-ray binaries may significantly contribute to the harder X-ray luminosity.

To estimate the amount of soft X-ray emission that may originate from hot gas heated by SNRs we make use of model results by Cioffi (1990, see also Junkes et al. 1990). These simulations assume a single SNR expanding into an interstellar medium (of typical density 1 cm^{-3}) and show that such an energy source produces an average luminosity of $7\cdot10^{37}$ erg s^{-1} in soft X-rays (>0.1 keV) for about $2\cdot10^4$ yrs. Using the estimated number of ~ 3750 SNRs in He 2-10 (derived from our radio observations) these SNRs hence can produce up to $\sim 2.6\cdot10^{41}$ erg s^{-1}. The large number of SNRs in He 2-10 therefore can easily explain the *ROSAT* detected X-ray luminosity, a result which further supports the idea that a significant part of the soft X-ray emission originates from hot gas in this BCDG.

4. Discussion

If we consider that the velocity feature at 250 km s^{-1} corresponds to the receding side of an inclined and open polar flow (whose approaching side is approximately at the systemic velocity of the galaxy) then, this value would correspond to a lower limit of its expansion velocity due to the geometry of this kind of flow (see Cuesta et al. 1995). This value of 250 km s^{-1} is a factor two larger than the expansion velocities found for well defined superbubbles in brighter and closer similar galaxies (Marlowe et al. 1995; Martin 1998), and would imply the presence of an extraordinary powerful outflow in He 2-10. The relation of this faint component with the low-intensity high-velocity wings observed in the central parts (500–600 pc) of the galaxy is still unknown, but can be interpreted as the blowout of this central high-velocity flow. On the other hand, if we assume that the line-splitting observed in the slit position at P.A. 49° corresponds to a second closed or almost closed polar superbubble, we find a velocity separation of 75 km s^{-1}.

Considering the mass of ionized gas involved in the bubble-like structures (calculated from the Hα integrated surface photometry of the shell structures) together with an assumed expansion velocity, it is possible to estimate a value for the kinetic energy involved in the powering of the superbubbles. If we assume an expansion velocity of 250 km s^{-1} for the flow and the total mass determined for the shells at the east and northeast of knot A, we obtain a kinetic energy of 13×10^{52} erg. In contrast, this value converts into 10^{52} erg if we assume an expansion velocity of 75 km s^{-1}. In both cases, the energy involved in the superbubble expansion is lower than 350×10^{52} erg, the energy that the 3750 SNRs that we have estimated in He 2-10 can eject into the surrounding interstellar medium. To this mechanical input we have to add the effect of the stellar winds of the massive stars of the starburst along their lifes. The contribution of the 6200 O5V stars we have estimated in the burst, assuming a stellar wind power per star of about 3.3×10^{36} erg s^{-1} (Leitherer 1998), and an age of 5×10^6 yr for the burst, results to be about 320×10^{52} erg, of the same order of the energy released by the SN explosions. The fact that the kinetic energy we have estimated for the bubbles is lower than the mechanical energy input by the massive star population could be due to, at least, three reasons: i) the measured ionized mass is a lower limit because it includes only the eastern part of the bubble (and only the part clearly detached from the bulk of the Hα emission around the star forming knots); ii) important radiative losses should be occuring in the expansion of these kiloparsec-scale superbubbles; iii) the superbubble has suffered a strong blowout and is, in part, expanding over the very low density intergalactic medium. In this sense, the presence of the apparently open polar flow expanding at very high velocities and the X-ray spurs suggest such blowout. On the other hand, the total mechanical luminosity released by SNRs+Winds is $\sim$4.1 $\times$ 10^{40} erg s^{-1}, of the same order of the X-ray luminosity, estimated to be in the range 8.5×10^{39}–8.5×10^{40} erg s^{-1}.

Adopting a linear size of $\sim$ 925 pc for the bubble like structures and following the models by Weaver, McCray & Castor (1977) and Shull (1993) we estimate a dynamical age of 2.2 Myr for the outflow structure in the case of assuming an expansion velocity of 250 km s^{-1} and of 11.1 Myr for a velocity of 50 km s^{-1}. Only the first case is consistent with the age of 5 Myr estimated for the central bursts (knot A and B).

Taking into account the dynamical mass estimations of the galaxy for different inclination angles by Kobulnicky et al. (1995) we derive a range of escape velocities between 110 and 425 km s^{-1} for inclination angles of 90° and 15° respectively. These values of the escape velocity are of the order of the largest ionized gas velocities reported and, therefore, the material associated with the high-velocity outflow could have sufficient energy to escape from the galaxy. This result reinforces the possibility of the presence of a blowout in He 2-10.

All the previous findings give an indication that there exists a bipolar outflow in the southwest-northeast direction of the WR BCDG He 2-10. This outflow presents an apparent bipolar shape probably including several individual shells or bubbles expanding at different velocities. Attending to energy considerations, these kinematic structures are likely to have been produced by the combined action of SNe and stellar winds from massive stars. The fact that the center of symmetry of this apparent bipolar structure coincides with the brightest knot A indicates that it is mainly powered by this object. We can not reject some contribution from the massive stellar population of knot B, that can be contributing to the complex kinematic and morphological behaviour of the flow. It is also interesting to point out that the major axis of the apparent bipolar structure is almost perpendicular to an imaginary line at P.A. 130°, that is the direction of the CO tail found by Kobulnicky et al. (1995) at the center of the galaxy and also the one of the near-infrared disk found by Beck et al. (1997) in the inner 20 ″. An interesting question arises: are these distributions focusing the apparent bipolar flow?.

5. Conclusions

We have carried out a multi-wavelength study: Hα and red continuum imaging, high resolution radio-continuum mapping at 6.3 and 3.5 cm, X-ray mapping and Hα high-resolution spectroscopy, of the WR BCDG He 2-10. Our main conclusions can be summarized as follows:

- The continuum-subtracted Hα image of He 2-10 shows the presence of a complex kiloparsec-scale bipolar superbubble centered on the most intense star forming knot (A) and whose main axis is almost perpendicular to an imaginary line at P.A. 130° (northeast-southwest direction).
- High-resolution spectroscopy of the bipolar feature shows a complex structure of possibly different kinematic components expanding with velocities in the range 50–250 km s^{-1}.
- According to radio-continuum observations, we derive an overall spectral index of α=$-$0.59$\pm$0.05 for He 2-10. We also note that the radio-continuum regions towards the east have significantly steeper spectra indicating that more non-thermal emission is concentrated there. These regions have no counterpart in our Hα or X-ray images. Comparing the total radio-continuum luminosity of He 2-10 with that of

the LMC we estimate a number of ∼3750 SNRs. These SNRs alone can easily explain the soft *ROSAT* detected X-ray emission. In addition we expect point-like sources to contribute significantly, especially to the harder X-ray emission. Considering an age of 5 Myr for the burst we estimate a SN rate of 1.9×10^{-3} SN yr^{-1}.

– The X-ray emission extends on a similar scale to the Hα emission. The extensions of the X-ray distribution towards northeast and southwest appear to be well spatially correlated with the position of the bipolar lobes indicating the hot gas is confined inside the bubbles. In contrast, there are two low-intensity extensions or spurs towards the northwest and southeast which are not correlated with the structures. These features could correspond to outflows or leakage of hot gas.
– The comparison between the energetics of the outflows and the expected mechanical energy released by the SNe and stellar winds indicates that the large-scale expanding structures can be powered by the massive star burst or SNe population of the galaxy and, therefore, can be considered as a galactic wind.
– Estimates of the escape velocity of the galaxy indicate that part of the large-scale outflows can escape the weak potential dwell of the galaxy, reinforcing the possibility of the presence of a blowout in He 2-10.

Acknowledgements. We are grateful to Romano Corradi for his valuable help during the IACUB observations at the NOT. We are also very grateful to Bob Sault for his help during the reduction process of the radio-continuum images with the MIRIAD program and to Manami Sasaki for her help in the X-ray reduction. We thank L. Cuesta for his help with the GRAFICOS program and for fruitful discussions about bipolar flows. We also thank Henry A. Kobulnicky and the anonymous referee for their valuable comments on different aspects of the paper. This research was partially funded through grant n^{o} PB 94-1108 from the Dirección General de Investigación Científica y Técnica of the Spanish Ministerio de Educación y Ciencia. The *ROSAT* project is supported by the Max-Planck-Gesellschaft and the Bundesministerium für Forschung und Technologie (BMFT). This research made use of the Karma software package devolped by the ATNF.

References

Allen D.A., Wright A.E., Goss W.M., 1976, MNRAS 177, 91
Beck S.C., Kovo O., 1999, AJ 117, 190
Beck S.C., Kelly D.M., Lacy J.H., 1997, AJ 114, 585
Calwell N., Phillips M.N., 1989, ApJ 338, 789
Cerviño M., Mas-Hesse J.M., 1994, A&A 284, 749
Cioffi D.F., 1990, In: Brinkmann W., Fabian A.C., Giovanelli F. (eds.) Physical Processes in Hot Cosmic Plasmas. NATO ASI Series C, Vol. 305, Kluwer, Dordrecht, p. 1
Conti P.S., 1991, ApJ 377, 115
Conti P.S., Vacca W.D., 1994, ApJ 423, L97
Corbin M.R., Korista K.T., Vacca W.D., 1993, AJ 105, 1313
Cram L., Hopkins A., Mobasher B., Rowan-Robinson M., 1998, ApJ 507, 155
Cuesta L., Phillips J.P., Mampaso A., 1995, A&A 304, 475
Davies R.I., Sugai H., Ward M.J., 1998, MNRAS 295, 43
Dahlem M., Petr M.G., Lehnert M.D., Heckman T.M., Ehle M., 1997, A&A 320, 731
de Vaucouleurs G., de Vaucouleurs A., Pence W., 1974, ApJ 194, L119
Dickow R., Hensler G., Junkes N., 1996, In: Kunth D., Guiderdoni B., Heydari-Malayeri M., Thuan T.-X. (eds.) The Interplay Between Massive Star Formation, the ISM and Galaxy Evolution. Editions Fronti res, Gif-sur Yvette, p. 583
Dufour R.J., Hester J.J., 1990, ApJ 350, 149
Esteban C., Peimbert M., 1995, A&A 300, 78
Gallagher J.S., Hunter D.A., Tutukov A.V., 1984, ApJ 284, 544
Haynes R.F., Klein U., Wayte S.R., et al., 1991, A&A 252, 475
Henize K.G., 1967, ApJS 126, 125
Hensler G., Dickow R., Junkes N., 1997, Rev. Mex. Astron. Astrofis. (Serie de Conferencias) 6, 90
Hog E., Baessgen G., Bastian U., et al., 1997, A&A 323, 57
Howarth I.D., Murray J., 1990, SERC Starlink User Note N$^{\circ}$ 50
Johansson L., 1987, A&A 182, 179
Junkes N., Zinnecker H., Hensler G., Dahlem M., Pietsch W., 1995, A&A 294, 8
Kennicutt R.C., 1988, ApJ 334, 144
Klein U., Weiland H., Brinks E., 1991, A&A 246, 323
Kobulnicky H.A., Dickey J.M., Sargent A.I., Hogg D.E., Conti P.E., 1995, AJ 110, 116
Kondratjeva L.N., 1972, Astron. Tsirk. 692, 1
Leitherer C., 1994, Rev. Modern Ast. 7, 73
Leitherer C., 1998, In: Aparicio A., Herrero A., Sánchez F. (eds.) Stellar Astrophysics for the Local Group. VIII Canary Islands Winter School of Astrophysics, Cambridge University Press, p. 527
Leitherer C., Heckman T.M., 1995, ApJS 96, 9
Marlowe A.T., Heckman T.M., Wyse R.F.G., Schommer R., 1995, ApJ 438, 563
Martin C.L., 1998, ApJ 506, 222
McKeith C.D., García López R.J., Rebolo R., et al., 1993, A&A 273, 331
Méndez D.I., Esteban C., 1997, ApJ 488, 652
Méndez D.I., Cairós L.M., Esteban C., Vílchez J.M., 1999, AJ in press
Meurer G.R., Freeman K.C., Dopita M.A., Cacciari C., 1992, AJ 103, 60
Meynet G., 1995, A&A 298, 767
Ohyama Y., Taniguchi Y., 1998, In: Van der Hucht K.A., Koenigsberger G., Eenens P.R.J. (eds.) Proc. IAU Symp. 193, Wolf-Rayet Phenomena in Massive Stars abd Starburst Galaxies. In press
Oke J.B., 1990, AJ 99, 1621
Papaderos P., Fricke K.J., to appear in: Aschenbach B., et al. (eds.) Proc. of Highlights in X-ray Astronomy. Garching, June 1998
Pérez-Olea D.E., Colina L., 1995, MNRAS 277, 857
Pfeffermann E., Briel U.G., Hippmann H., et al., 1986, Proc. SPIE 733, 519
Pietsch W., Trinchieri G., Vogler A., 1998, A&A 340, 351
Pottasch S.R., 1984, Planetary Nebulae. D. Reider Publishing Company, p. 92
Sargent W.L.W., Searle L., 1970, ApJ 162, L155
Sault B., Killeen N., 1998, MIRIAD Users Guide, ATNF
Sauvage M., Thuan T.X., Lagage P.O., 1997, A&A 325, 98
Shull J.M., 1993, In: Cassinelli J.P., Churchwell E.B. (eds.) Massive Stars: Their Lives in the Interstellar Medium. ASP, San Francisco, p. 327
Stevens I.R., Strickland D.K., 1998, MNRAS 294, 523
Sugai H., Taniguchi Y., 1992, AJ 103, 1470
Trümper J., 1983, Adv. Space Res. 2, No. 4, 241
Vacca W.D., Conti P.S., 1992, ApJ 401, 543
Wang J., Heckman T.M., Weaver K.A., Armus L., 1997, ApJ 474, 659
Weaver R., McCray R., Castor J., 1977, ApJ 218, 377